



Ni/YSZ electrodes structures optimized for increased electrolysis performance and durability

Hauch, Anne; Brodersen, Karen; Chen, Ming; Mogensen, Mogens Bjerg

Published in:
Solid State Ionics

Link to article, DOI:
[10.1016/j.ssi.2016.06.003](https://doi.org/10.1016/j.ssi.2016.06.003)

Publication date:
2016

Document Version
Peer reviewed version

[Link back to DTU Orbit](#)

Citation (APA):
Hauch, A., Brodersen, K., Chen, M., & Mogensen, M. B. (2016). Ni/YSZ electrodes structures optimized for increased electrolysis performance and durability. *Solid State Ionics*, 293, 27-36.
<https://doi.org/10.1016/j.ssi.2016.06.003>

General rights

Copyright and moral rights for the publications made accessible in the public portal are retained by the authors and/or other copyright owners and it is a condition of accessing publications that users recognise and abide by the legal requirements associated with these rights.

- Users may download and print one copy of any publication from the public portal for the purpose of private study or research.
- You may not further distribute the material or use it for any profit-making activity or commercial gain
- You may freely distribute the URL identifying the publication in the public portal

If you believe that this document breaches copyright please contact us providing details, and we will remove access to the work immediately and investigate your claim.

Ni/YSZ electrodes structures optimized for increased electrolysis performance and durability

A. Hauch^{1*}, K. Brodersen¹, M. Chen¹, M.B. Mogensen¹

¹ Department of Energy Conversion and Storage, Technical University of Denmark, Risø Campus, Frederiksborgvej 399, DK-4000 Roskilde, Denmark.

* Corresponding author. Tel.: +4521362836. Fax: +4546775858.

E-mail: hauc@dtu.dk

Abstract

Cermet Ni/YSZ electrodes are the most commonly applied fuel electrode for solid oxide cells (SOC) both when targeting solid oxide fuel cell (SOFC) applications and when used as solid oxide electrolysis cell (SOEC).

In this work we report on the correlation between initial Ni/YSZ microstructure and the resulting electrochemical performance both initially and during long-term electrolysis testing at high current density and high $p(\text{H}_2\text{O})$ inlet. Especially, this work focuses on microstructure optimization to hinder Ni mobility and migration during long-term operation and illustrates the key-role of electrode over-potential on the degradation of the Ni/YSZ electrodes in SOEC. We find that for long-term stability for electrolysis at high current densities and high $p(\text{H}_2\text{O})$ the as-produced NiO/YSZ precursor electrode should be: 1) As dense as possible, 2) as fine particle and pore sized as possible and 3) the three phases (Ni, YSZ and pore phase) shall be size-matched and well-dispersed. Applying such microstructure optimized Ni/YSZ electrode we show SOEC test results with long-term degradation rate as low as 0.3-0.4 %/kh at -1 A/cm^2 , $800 \text{ }^\circ\text{C}$ and inlet gas mixture of $p(\text{H}_2\text{O})/p(\text{H}_2):90/10$. This enables SOEC operation of such cell for more than 5 years below thermo-neutral potential at these operating conditions.

Keywords

Solid Oxide Electrolysis Cells, Ni/YSZ electrode, microstructure, electrochemical impedance spectroscopy, performance, durability

1. Introduction

Solid oxide electrolysis cells (SOEC) can play an important role in the future energy grid based on increased share of renewable energy. SOEC can then be applied to store surplus electrical energy e.g. from wind turbines via hydrogen production (when SOEC are used for electrolysis of H_2O) or for syn-gas production (when SOEC are used for electrolysis of $\text{CO}_2 + \text{H}_2\text{O}$) and subsequent synthetic natural gas production or production of other synthetic fuels. The SOEC technology offers the most efficient electrolysis technology for conversion of electrical energy and the possibility for syn-gas production [1] or even direct methane production at lower temperature and pressurized operation [2].

However, for a commercial break-through for the SOEC technology not only high initial performance is required, but also long-term stability preferably in a large range of operating conditions (temperature, gas compositions, current densities etc.) is a necessity combined with inexpensive materials and processing techniques. Based on economic analyses lifetime of at least 5 years of operation around thermo-neutral potential is desirable at highest possible current density (fuel production rate) [3]; not necessarily operated at maximum current density throughout its lifetime but for shorter or longer periods of time depending on grid balancing requirements. Even though reversible operation of SOC (i.e. fuel cell mode operation) has shown advantageous for the performance of SOC [4,5]; it should be emphasized that at higher electrolysis current densities irreversible degradation phenomena takes place which are not likely to be recoverable by SOFC operation of the SOC [6,7].

Long-term stability needs to be improved even considering promising results such as reported by Tietz, Corre and Hjalmarsson [8–11] if SOFC systems, and later SOEC systems, are to operate profitable for several years. Recent work has shown that at high current density (high fuel electrode overpotential) the SOEC experiences long-term, roughly linear, irreversible degradation; typically associated with an increase in the ohmic resistance [7,8,12]. Post-mortem microscopy investigations of these long-term tested cells show irreversible damages of the Ni/YSZ microstructure; e.g. decrease in the Ni-YSZ contact area, loss of Ni percolation (loss of Ni-Ni contact) and even migration of Ni away from the few micrometer of the fuel electrode closest to the electrolyte [7,8,12]. These degradation phenomena relating to the Ni/YSZ microstructure have been shown to be associated with 1) impurity inclusions in and around Ni particles [13], 2) formation of ZrO_2 nano-particles [7], 3) Ni particles morphology changes and coarsening and 4) Ni migration [7,8,12].

The aim of this work is to investigate and optimize the Ni/YSZ electrode microstructure to ensure high performance and long-term stability of the Ni/YSZ electrode during electrolysis operation at high $p(\text{H}_2\text{O})$ and high current density. This is targeted via hindering or at least limiting Ni migration and mobility. We report microstructural and electrochemical test results for SOEC with three intentionally different initial Ni/YSZ electrode microstructures but tested at nominally the same electrolysis test conditions. Furthermore, the results show that it is hardly the “externally”

set test conditions that sets the threshold for initiating the irreversible microstructural changes of the Ni network. Rather, the electrode over-potential is a key parameter for the onset of the damaging and irreversible loss of performance for the Ni/YSZ-based SOEC electrodes.

2. Experimental

2.1. Cell Specifications and Test Set-up

The cells used for electrolysis testing in this study are fuel electrode supported full SOEC. The cells are Ni/YSZ supported Ni/YSZ-YSZ-CGO_{barrier}-LSC/CGO based cells produced at DTU Energy [14]. An overview of cell and test specifications is given in Table 1. The cells consisted of a 12-16 μm thick Ni/YSZ fuel electrode (not for Cell A) with a ~ 300 μm thick Ni/YSZ support layer, a ~ 10 μm thick YSZ electrolyte, a 6-7 μm thick CGO barrier layer and a ~ 30 μm thick LSC/CGO oxygen electrode [15]. No active fuel electrode was applied in Cell A. The porous and coarser ~ 300 μm thick Ni/YSZ support layer therefore also acted as active fuel electrode in Cell A. Zirconia stabilized with 8 mole percent Y_2O_3 was used for the electrolyte and the active fuel electrode layers. Zirconia stabilized with 3 mole percent Y_2O_3 was used for the support layer [3,16,17]. For all applied Ni/YSZ cermets the quantities of NiO and YSZ were scaled to provide a Ni/YSZ volume ratio of 40/60 after reduction of NiO. For the production of the support layer, active fuel electrode, electrolyte and CGO barrier layer successive tape casting i.e. a multilayer tape casting (MTC) process and lamination process was applied [14]. These four MTC layers of the tapes were cut into 16×16 cm^2 pieces and co-sintered at 1315 $^\circ\text{C}$ [18] and then cut into 53×53 mm^2 cells. The oxygen electrode (40×40 mm^2) was applied by screen-printing and sintered at 930 $^\circ\text{C}$. Afterwards, a LSM contact layer was applied by screen-printing. The set-up for single cell testing was illustrated and described in detail previously [19,20], and the set-up illustrated as “*Cell assembly 2*” in the work by Ebbesen and co-workers was applied in this work [20]. Long-term galvanostatic electrolysis tests were conducted for all cells (Table 1) but for each cell type a “sister-cell” was also reduced but not long-term tested to provide a reference cell for investigation of initial microstructures.

2.2. Test Procedure and Operating Conditions

The cells were heated (1 $^\circ\text{C}/\text{min}$) to 850 $^\circ\text{C}$ for sealing and the NiO was reduced by leading 20 l/h of dry 9% H_2 in N_2 to the fuel electrode for 2 hours followed by 1 hour of 20 l/h dry H_2 to the fuel electrode while air was led to the oxygen electrode [21]. This reduction procedure was chosen to make the NiO reduction procedure similar to several previously reported SOEC test (e.g. [7,10,12]) and kept constant as previously reported results of 3D reconstructions of fuel electrodes show that the reduction profile can affect the fuel electrode microstructure significantly [22]. Hereafter performance characterization via iV-curves and electrochemical impedance spectroscopy (EIS) was conducted. This performance characterization was done at 850 and 800 $^\circ\text{C}$ and included

characterization at different gas composition to the electrodes (air/oxygen to the oxygen electrode and 4, 20 and 50 % H₂O in H₂ to the fuel electrode). Subsequently the galvanostatic steam electrolysis tests were initiated and the test conditions were: 800 °C, inlet p(H₂O)/p(H₂):90/10; 56 % H₂O conversion, oxygen led to the oxygen electrode and a current density of -1 A/cm^2 for Cell A, B and C; but -1.25 A/cm^2 for Cell D. After ending of each long-term test, the cell performances were again measured via iV-curves and EIS at OCV applying different gas compositions and temperature prior to cooling down in dry H₂.

2.3. Electrochemical Impedance Spectroscopy (EIS)

A Solartron 1255 frequency analyzer was used for recording EIS both at OCV during initial and final characterization but also during electrolysis testing applying a set-up as described by Jensen [23]. Impedance spectra (IS) were recorded with 12 points/decade in the frequency range from 97 kHz to 0.1 Hz. The in-house developed Python-based software Ravdav was used for plotting and analysis of the impedance data [24]. In this work, experimentally obtained impedance spectra are depicted as inductance corrected data in Nyquist plot and imaginary part of Bode plot. Furthermore, plots of distribution of relaxation times (DRT) are provided. The DRT plots are used to illustrate development of impedance over time and to highlight frequency ranges for different processes contributing to the total impedance response from the cells [25,26]. To enable a quantitative analysis of the IS complex-non-linear-least-squares (CNLS) method was used to fit an equivalent circuit model to the data. For a quantitative break-down of losses via IS the equivalent circuit based on the work reported by Kromp et al. [27] was used. Here the electrochemical impedance response from the Ni/YSZ electrode was approximated by two RQ-elements. The higher frequency impedance arc (RQ)_{ionic} at $\sim 10\text{-}40 \text{ kHz}$ has previously been ascribed to ionic transport through the ionic conducting matrix in the electrodes. For the applied cells (Ni/YSZ-YSZ-LSC/CGO) with the mixed ionic electronic and highly conducting LSC based oxygen electrode, the majority of the resistance, R_{ionic}, can be expected to originate from the Ni/YSZ electrode. The (RQ)_{Ni/YSZ,TPB} at $\sim 1\text{-}4 \text{ kHz}$ is ascribed to the electrochemical process at the triple phase boundaries (TPBs). These contributions to the overall impedance of the cell can also be described in more detail via a transmission line model (TLM) for the impedance response [26,28,29]. The impedance response from the LSC/CGO oxygen electrode has been approximated by a Gerisher-type response in the CNLS fitting routine in line with the work by Hjelm et al. [15]; having a characteristic frequency of $\sim 100 \text{ Hz}$. Furthermore; gas diffusion and gas conversion resistance contributions as described by Primdahl and Mogensen have been approximated by two RQ-circuits having characteristic frequencies around $\sim 40 \text{ Hz}$ and $\sim 2 \text{ Hz}$, respectively [30,31]. “Estimated uncertainty for the resistance values obtain via equivalent circuit modeling of IS $\sim \pm 4 \text{ m}\Omega\text{cm}^2$. This is based on comparison of equivalent circuit modeling results for initial characterization of long-term tested cells and their corresponding non-long-term tested “sister-

cells” as well as analysis of differences between experimental and simulated values for Z_{real} and Z_{imag} as function of frequency.”

2.4. SEM imaging

Pieces of a cross section length of ~ 1 cm of the reference cells and the long-term tested cells were prepared for SEM investigations by vacuum embedding in epoxy (EpoFix from Struers[®]) followed by grinding and polishing. A Zeiss Supra 35 FE-SEM (Field Emission Gun Scanning Electron Microscope) was used for imaging. SEM images obtained at 8-10 kV using the secondary electron detector and low-voltage SEM images were obtained at 0.9 kV using the in-lens detector. Low-voltage in-lens SEM imaging allows percolating and non-percolating Ni to be distinguished in the Ni/YSZ cermet microstructure, as described by Thydén et al. [32] and later illustrated several times for long-term tested SOC [7,33–35]. Image analysis by line-intercept-method [36] allowed for determination of the area fraction and particle size distributions of Ni and pores, using the in-house developed Matlab based software, ManSeg. For each sample, images at a magnification of 4 kX were used for these analyses of the fuel electrode/electrolyte interfaces and at least 1500 μm interface was investigated for each cell. The particle size distributions (PSD) based on this line intercept method [36] are given as upper limit values for mean-intercept-lengths in intervals of 50 nm and an illustration of the mean-intercept-line method can be found elsewhere [5]. This method of analysis can lead to an over-estimate of Ni fraction and size due to larger effect of smearing of Ni compared to the hard ceramic YSZ during sample preparation. A similar quantification as for the Ni and pore phase using this mean-intercept-length method is not included for the YSZ phase. The YSZ phase of these sintered structures are very little suitable for this type of analysis due to the edgier and more angular shape of the YSZ particles. This leads to more “planar” interphases between YSZ grains and makes it hard and often too subjective to decide when YSZ particles are separate particles or sintered into a particle that should be considered one YSZ particle.

Table 1: Cell and test specifications for Cell A, B, C and D.

Name	Cell specifications	Qualitative microstructure information	Test specifications
Cell A	No specific fuel electrode layer. Support layer functioning as fuel electrode (Ni/3YSZ)	Coarse structure. Significantly higher pore fraction than Cell B, C and D	800 °C, p(H ₂ O)/p(H ₂):90/10, 56 % H ₂ O conversion, -1 A/cm ² , 1000 h
Cell B	Support layer (Ni/3YSZ) and active fuel electrode layer (Ni/8YSZ)	Coarse microstructure. As dense as possible for a Ni/YSZ:40/60 fuel electrode.	800 °C, p(H ₂ O)/p(H ₂):90/10, 56 % H ₂ O conversion, -1 A/cm ² , 1000 h

Cell C	Support layer (Ni/3YSZ) and active fuel electrode (Ni/8YSZ)	Fine microstructure. As dense as possible for a Ni/YSZ:40/60 fuel electrode.	800 °C, p(H ₂ O)/p(H ₂):90/10, 56 % H ₂ O conversion, -1 A/cm ² , 2000 h
Cell D	Sister-cell to cell C	Fine microstructure. As dense as possible for a Ni/YSZ:40/60 fuel electrode.	800 °C, p(H ₂ O)/p(H ₂):90/10, 56 % H ₂ O conversion, -1.25 A/cm ² , 1000 h

3. Results

3.1. Initial microstructures

Figure 1 shows the initial microstructures for the three types of fuel electrodes produced for this study. Representative SEM images at two different magnifications are shown for the three types of microstructures. The intention was to create three different microstructures all produced via tape casting and co-sintering with the different layer of the fuel electrode half-cell and this was successfully obtained. In Figure 1 the Ni particles visually appears as if they are on top of the YSZ skeleton and scratches, as a consequence of mechanical polishing, are visible in the Ni particles but not in the YSZ. Furthermore, EDS was used on a regular basis to confirm the distinguishing between the Ni and YSZ phases for SEM images as those presented in Figure 1. The microstructure of Cell A is coarse with average mean intercept length of Ni particles of $\sim 1.3 \mu\text{m}$. The porosity in the as-produced electrode was introduced by tailoring the particle size by optimizing the milling procedure and addition of fractions of calcined 3YSZ in the slurry for the electrode of Cell A. After reduction of NiO; this fuel electrode had a porosity of $\sim 36 \%$. Cell B has Ni particle sizes rather close to those for Cell A; $\sim 1.3 \mu\text{m}$; but the active fuel electrode layer is denser and has a pore fraction after reduction of NiO close to the theoretical value of 21.8 % originating from reduction of NiO in an electrode with a volume ratio of Ni/YSZ:40/60 (Table 2). Cell C has a porosity close to that of Cell B, however Cell C has a significantly different Ni particle size distribution. For Cell C the Ni mean-intercept-length was reduced to $\sim 0.8 \mu\text{m}$ (Table 2) and furthermore Cell C has a more narrow Ni-size distribution as illustrated via the Ni particle size distributions (PSDs) in Figure 2. Key numbers from the quantitative analysis are given in Table 2. Furthermore, Figure 2 shows that the best size-matching of Ni particles and pores was obtained for Cell C.

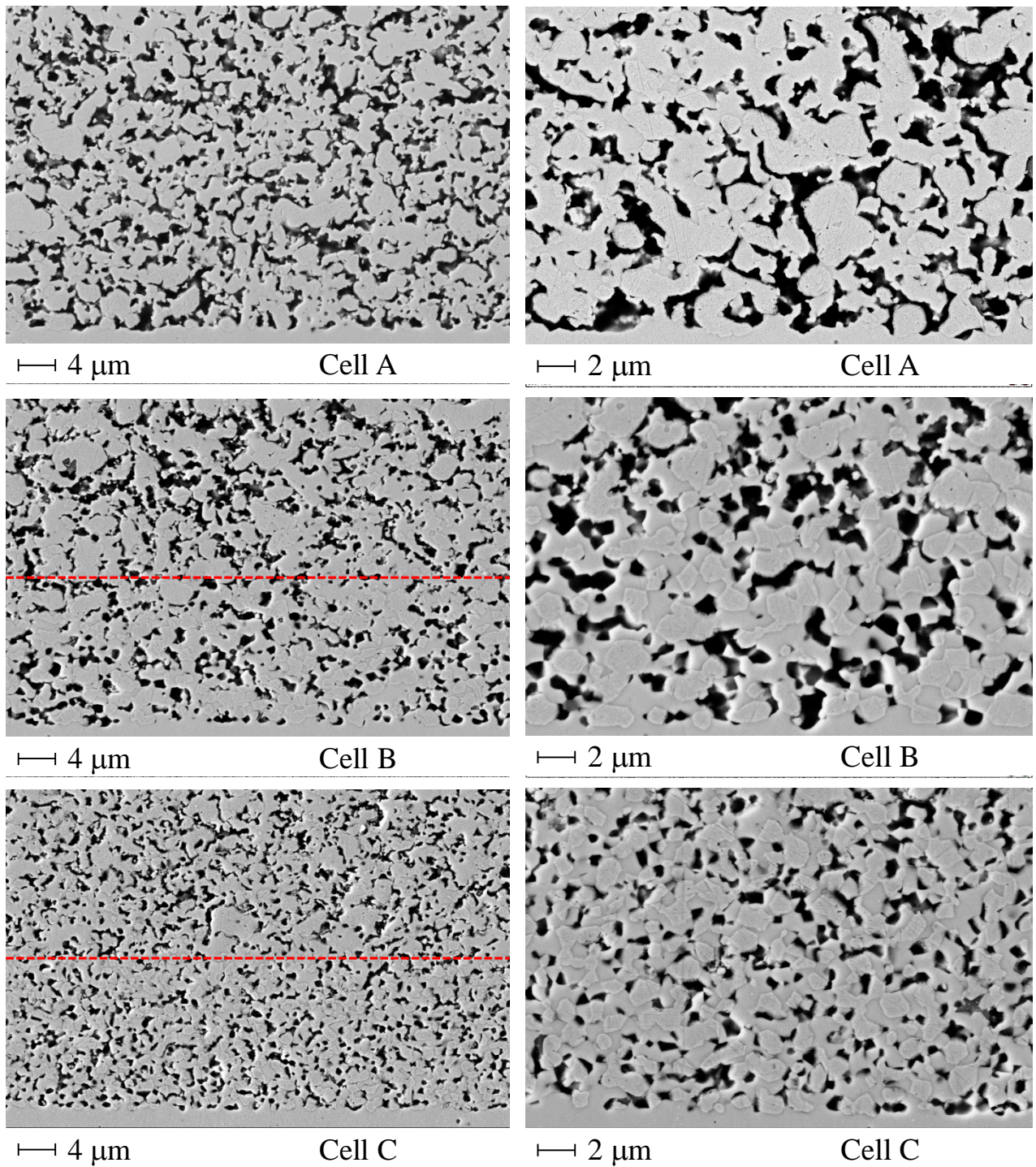


Figure 1: Initial Ni/YSZ microstructures for Cell A, Cell B and Cell C. The electrode/electrolyte interface is in the bottom of each image. For Cell B and Cell C, where different tapes were applied for active fuel electrode and support layer, dotted lines mark the border between the two layers.

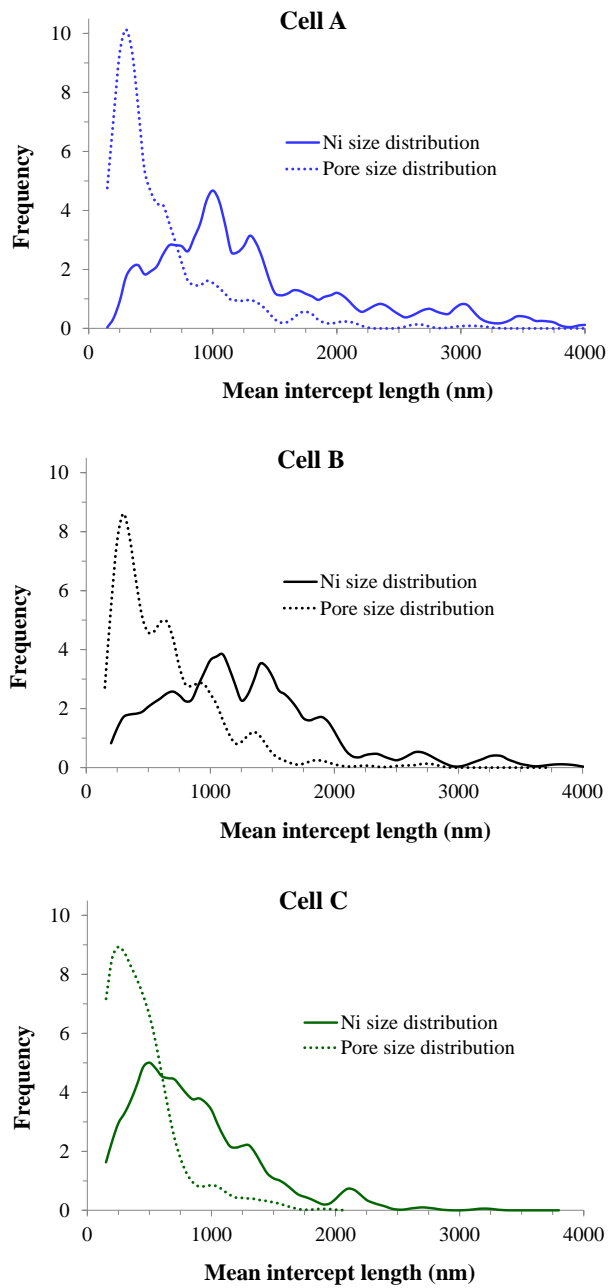


Figure 2: Ni and pore size distributions for Cell A, Cell B and Cell C for the fuel electrode structures 1-2 μm from the electrolyte. Each PSD is based on mean-intercept-lengths measured along a line of at least 1500 μm fuel electrode for each cell. The distributions are based on the line-intercept method [36] and the given numbers refer to upper limit values for mean-intercept-lengths divided into intervals of 50 nm.

Table 2: Characteristic numbers from quantitative analysis of SEM images of the initial Ni/YSZ electrode structure for Cell A, Cell B and Cell C. This method of analysis can lead to an over-estimate of Ni fraction and size due to larger effect of smearing of Ni compared to the hard ceramic YSZ during sample preparation. However, the results are comparable with each other for Cell A, Cell B and Cell C. A 3D reconstruction of Cell C resulted in Ni/YSZ/pore volume ratios of 31/49/20 giving a Ni/YSZ ratio of 39/61; close to the target of 40/60 set during preparation of the slurry for the Ni/YSZ electrode [37].

	Cell A	Cell B	Cell C
No of Ni/1000 μm interface	207	296	444
No of pores/1000 μm interface	363	398	528
Average Ni mean-intercept-length [nm]	1348	1225	832
Ni area fraction	0.28	0.34	0.35
Pore area fraction	0.36	0.23	0.21
YSZ area fraction	0.36	0.43	0.44

3.2. Long-term testing of SOEC with different Ni/YSZ microstructures

Long-term galvanostatic steam electrolysis tests were conducted for Cell A, Cell B and Cell C; all operated at 800 °C, inlet $p(\text{H}_2\text{O})/p(\text{H}_2):90/10$; 56 % H_2O conversion, O_2 to the oxygen electrode and a current density of -1 A/cm^2 . Figure 3 shows the cell voltage, ohmic resistance and total polarization resistance development over the electrolysis test periods. The cells did not have identical electrolyte and barrier layer thicknesses, which led to different ohmic resistances at start of test. To ease the comparison of the development of the ohmic resistance during electrolysis testing, Figure 3 also includes a plot where the ohmic resistances for Cell A and B were subtracted 10 and 47 $\text{m}\Omega\text{cm}^2$, respectively, to provide the same ohmic resistance at start of test as measured for Cell C. The difference in the initial ohmic resistances originates from different electrolyte and barrier layer thicknesses for the three cells¹ and therefore not believed to influence the subsequent development in ohmic resistances, which relates to microstructural changes in the Ni/YSZ electrode (Figure 6).

From the results depicted in Figure 3 it is noticed that all three cells experience an initial increase in polarization resistance over the first few hundred hours of test followed by a stabilization of the polarization resistance. Both Cell A and Cell B experienced a huge increase in the ohmic resistance and this did not seem to level off after several hundred hours of testing, which in turn will be detrimental to the cells. This is much in line with observations reported previously for electrolysis testing at high current densities [6,7,38]. Cell C, on the other hand, have an ohmic resistance development that was significantly different even though these three cells are tested at nominally

¹ By SEM imaging the following thicknesses for the barrier and the electrolyte layers were found; 5.7 μm for the barrier layer and 8 μm for the electrolyte for Cell A, 7 μm for the barrier layer and 10 μm for the electrolyte for Cell B, and 4 μm for the barrier layer and 8 μm for the electrolyte for Cell C. The thickness variation within a specific layer in a cell is kept around $\pm 0.5 \mu\text{m}$.

the same electrolysis test conditions. The ohmic resistance for Cell C only increase $7.5 \text{ m}\Omega\text{cm}^2/\text{kh}$ while the increase in the ohmic resistance for Cell A and B was 125 and $68 \text{ m}\Omega\text{cm}^2/\text{kh}$; respectively. From a technology focused “5-years-of-operations”-perspective this ohmic resistance increase will be the detrimental degradation cause for cells like Cell A and Cell B. The general trends for the ohmic resistances and polarization resistances as given in Figure 3 have been consolidated by several other long-term electrolysis test, of which a total of 10 long-term tests (1 kh) were conducted at the same electrolysis test conditions as for Cell A, Cell B and Cell C.

To provide a more detailed view on the increase of the resistances during electrolysis operation; IS recorded at the start, mid-way and at the end of the test of Cell A, B and C is given in Figure 4 including the corresponding DRT. Table 3 summarizes the key results for resistance contributions and characteristic frequencies obtained from CNLS fitting of the experimental data shown in Figure 4. Figure 5 gives a representative illustration of experimental data and the simulated IS including illustration of the individual resistance contributions for IS recorded at start and end of test of Cell B.

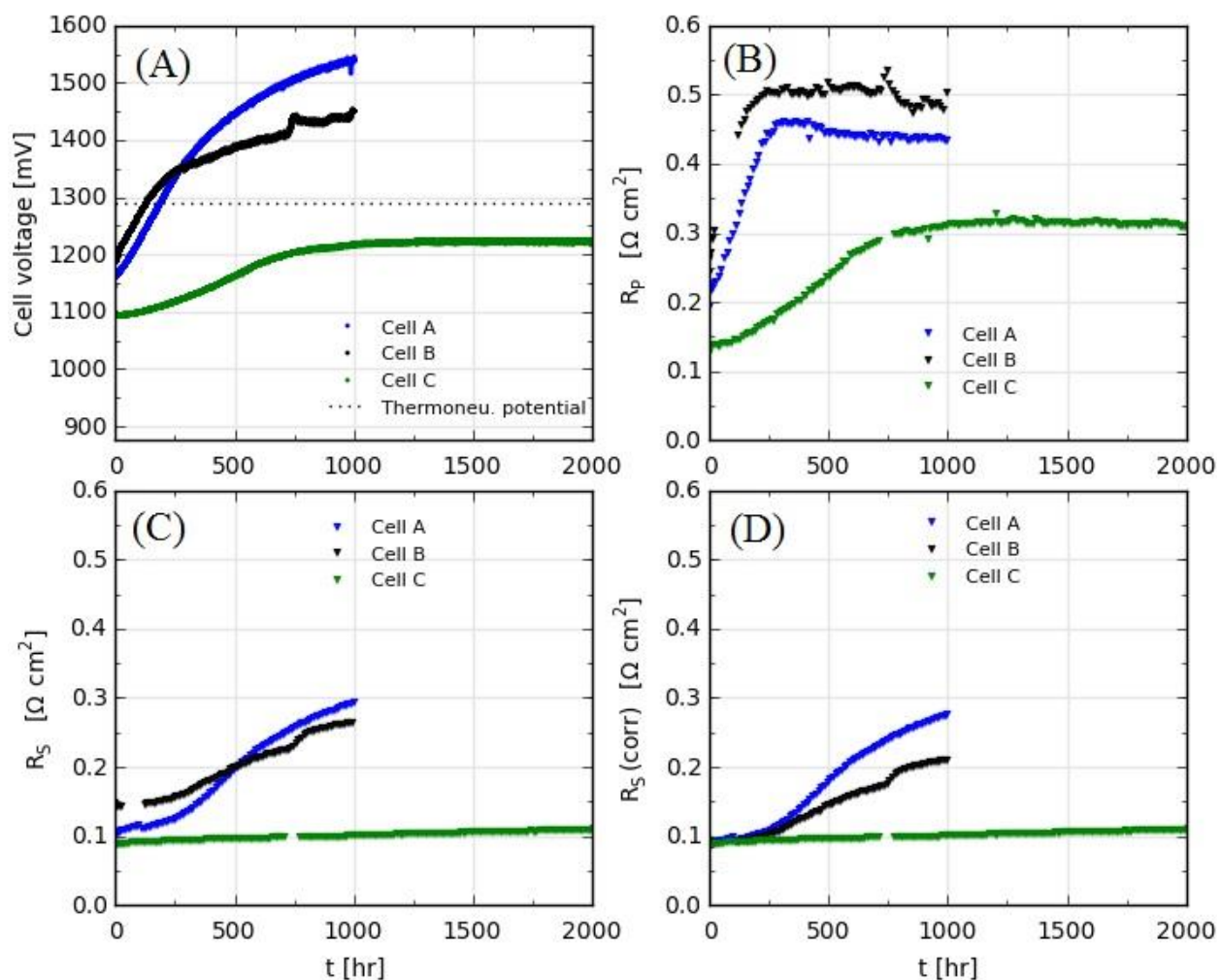


Figure 3: Galvanostatic long-term electrolysis testing of Cell A, Cell B and Cell C at -1 A/cm^2 , $800 \text{ }^\circ\text{C}$, O_2 to the oxygen electrode and a $p(\text{H}_2\text{O})/p(\text{H}_2)$ inlet with a ratio of 90/10 and a flow corresponding to 56 % steam conversion. A) Cell voltages over time, B) Total polarization resistances (R_p) over time, C) Ohmic resistances (R_s) over time and D) Ohmic resistances (R_s) over time where R_s for Cell A and B were subtracted 10 and 47 $\text{m}\Omega\text{cm}^2$, respectively.

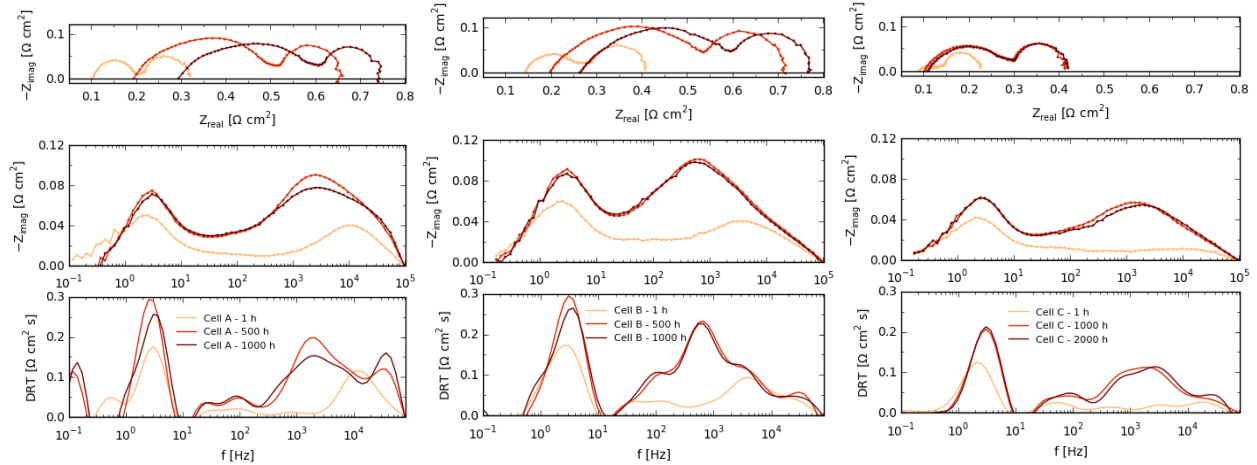


Figure 4: Nyquist (top), imaginary part of Bode (middle) and DRT plot (bottom) of IS recorded at start, half way through and at end of electrolysis test for Cell A (left), Cell B (middle) and Cell C (right). All tests and the depicted IS were conducted and recorded at -1 A/cm^2 , $800 \text{ }^\circ\text{C}$, inlet $p(\text{H}_2\text{O})/p(\text{H}_2):90/10$ and 56 % steam conversion. Notice that test of Cell A and B had duration of 1000 h for each but test of Cell C had a duration of 2000 h.

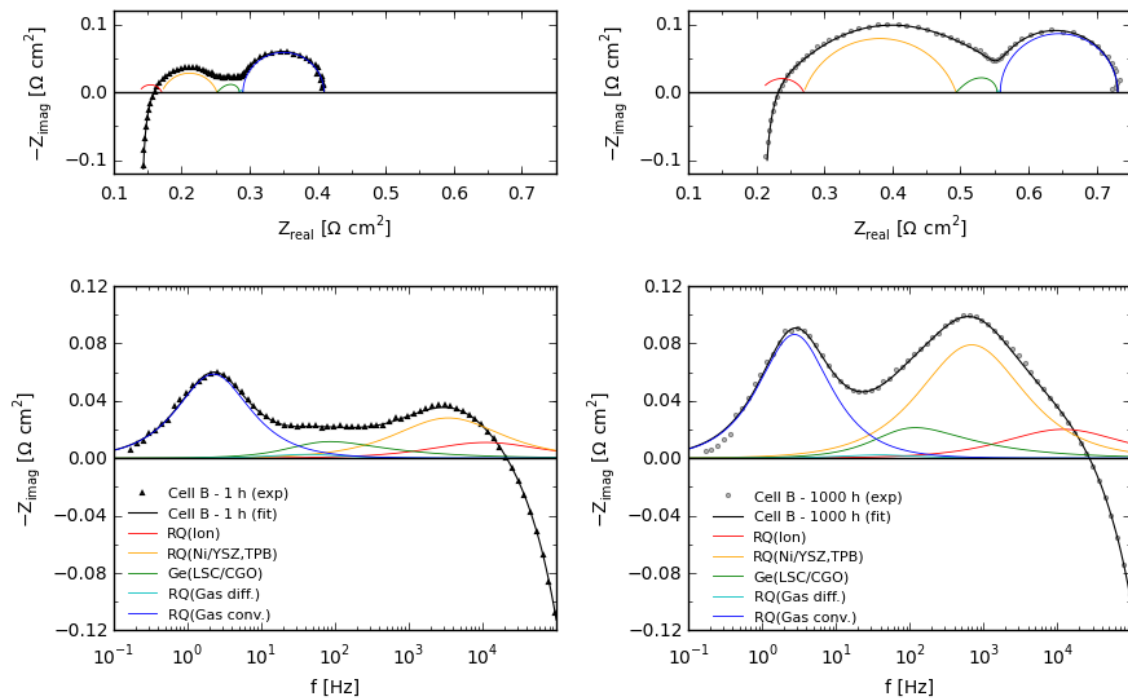


Figure 5: Illustration of experimental data and simulated IS based on the equivalent modeling fit for IS recorded after 1 h and 1000 h of test for Cell B. IS were recorded during long-term electrolysis testing i.e. at -1 A/cm^2 , $800 \text{ }^\circ\text{C}$, inlet $p(\text{H}_2\text{O})/p(\text{H}_2):90/10$ and 56 % steam conversion.

Table 3: Results from equivalent circuit modeling of IS recorded for Cell A, Cell B and Cell C during long-term steam electrolysis test at identical test conditions (-1 A/cm^2 , $800 \text{ }^\circ\text{C}$, inlet $p(\text{H}_2\text{O})/p(\text{H}_2):90/10$ and 56 % steam conversion). The applied model was described in the “Experimental” section. Estimated uncertainty for the resistances is $\sim \pm 4 \text{ m}\Omega\text{cm}^2$.

Time (h)	Cell A			Cell B			Cell C			
	0	500	1000	0	500	1000	0	500	1000	2000
$R_s \text{ (}\Omega\text{cm}^2\text{)}$	0.101	0.149	0.226	0.138	0.189	0.206	0.091	0.093	0.098	0.106
$R_{\text{ion}} \text{ (}\Omega\text{cm}^2\text{)}$	0.043	0.198	0.227	0.033	0.072	0.064	0.014	0.024	0.027	0.027
$f_{\text{ion}} \text{ (Hz)}$	15223	20778	33000	11067	10879	12045	14828	13150	13262	13396
$R_{\text{Ni/YSZ,TPB}} \text{ (}\Omega\text{cm}^2\text{)}$	0.055	0.138	0.125	0.081	0.234	0.224	0.024	0.079	0.130	0.128
$f_{\text{Ni/YSZ,TPB}} \text{ (Hz)}$	8178	1884	1632	3448	634	692	2528	2982	1525	1930
$R_{\text{LSC/CGO}} \text{ (}\Omega\text{cm}^2\text{)}$	0.014	0.031	0.029	0.033	0.041	0.060	0.015	0.030	0.038	0.037
$f_{\text{LSC/CGO}} \text{ (Hz)}$	97	99	105	87	126	120	93	116	137	131
$R_{\text{Gas diff.}} \text{ (}\Omega\text{cm}^2\text{)}$	0.005	0.003	0.005	0.005	0.007	0.005	0.003	0.004	0.004	0.004
$f_{\text{Gas diff.}} \text{ (Hz)}$	40	39	43	42	54	40	34	45	46	46
$R_{\text{Gas conv.}} \text{ (}\Omega\text{cm}^2\text{)}$	0.104	0.134	0.128	0.119	0.171	0.176	0.081	0.104	0.117	0.118
$f_{\text{Gas conv.}} \text{ (Hz)}$	2	3	3	2	3	3	2	2	3	3

From Figure 4 and Table 3 it is evident that the high frequency R_p contribution mainly from the fuel electrode (R_{ion}) contributes significantly and throughout the test period to the R_p increase for Cell A. This effect is ascribed to the fact that Cell A has a fuel electrode with an YSZ skeleton based on the lower ion conducting 3YSZ instead of the 8YSZ used for the fuel electrodes of Cell B and C. The fuel electrode for Cell A is the coarse Ni/3YSZ cermet typically applied as fuel electrode support layer. This in turn means that if the cell degrades in such a way that the oxide ions conducted through the electrolyte needs to be conducted further out in the fuel electrode to reach an active TPB site then this transport of oxide ions will lead to a higher resistance (R_{ion}) in Cell A compared to Cell B and Cell C.

For all three cells $R_{\text{Ni/YSZ,TPB}}$ increases during the first half of the tests and then stabilizes. Furthermore, the characteristic frequency, $f_{\text{Ni/YSZ,TPB}}$, decreases significantly for the highly degrading Cell A and B.

The numbers in Table 3 for $R_{\text{LSC/CGO}}$ indicate that the oxygen electrode degrades for all three cells. However, the numbers for the development in $R_{\text{LSC/CGO}}$ provided in Table 3 should be taken with some precaution, as the increase in $R_{\text{LSC/CGO}}$ might not only be related to the electrochemical performance of the oxygen electrode. It can also partly be due to: 1) The $R_{\text{Ni/YSZ,TPB}}$ increases and its characteristic frequency decrease and these contributions to the total polarization resistance are therefore less easily separable upon CNLS fitting of the data; and 2) as the fuel electrode degrades, regions of the active Ni/YSZ electrode is no longer electrochemically active (see Figure 6), current paths and distribution will change and thereby possibly also effect the measured overall oxygen

electrode performance. In principle analysis of differences in impedance spectra (ADIS, [19]) by varying gas compositions to the two electrodes, one at a time, could provide further information with respect to attributing impedance contributions to the specific electrode. However, the high performing LSC/CGO electrode only exhibit very limited sensitivity in impedance response towards changes in $p(\text{O}_2)$. The gas changes between air and oxygen done for these cells only provides a hint of appropriate characteristic frequency for the main impedance contribution from this electrode to the total impedance of the cells and the data is not useable for quantification purposes.

The gas diffusion resistance is small, almost negligible. The justification of including this contribution upon CNLS fitting of the experimental IS is based on previous work e.g. with SOC having different support layer microstructures [18].

3.3. Microstructures of long-term tested SOEC with different Ni/YSZ microstructures

Figure 6 shows the fuel electrode/electrolyte interface for Cell A and Cell C after electrolysis testing for 1000 h and 2000 h, respectively. For Cell A there is a significant lack of percolating Ni in the innermost $\sim 5 \mu\text{m}$ of the fuel electrode (Figure 6b). The structure of this innermost $\sim 5 \mu\text{m}$ of the fuel electrode seem an increased number of large pores; more than $1 \mu\text{m}$ diameter (Figure 6a) when compared to the initial structure for this fuel electrode (Figure 1a). In contrast, the fuel electrode/electrolyte interface for Cell C still contains a high density of Ni in a percolating network in the innermost $\sim 5 \mu\text{m}$ of the fuel electrode after electrolysis testing for 2000 h. Here it is worth noticing that the two cells depicted in Figure 6 were exposed to identical “externally” set test conditions with respect to temperature, gas compositions, flow rates and current density. The majority of Cell B was oxidized during the end characterization and SEM images of this sample is therefore not as illustrative as for Cell A.

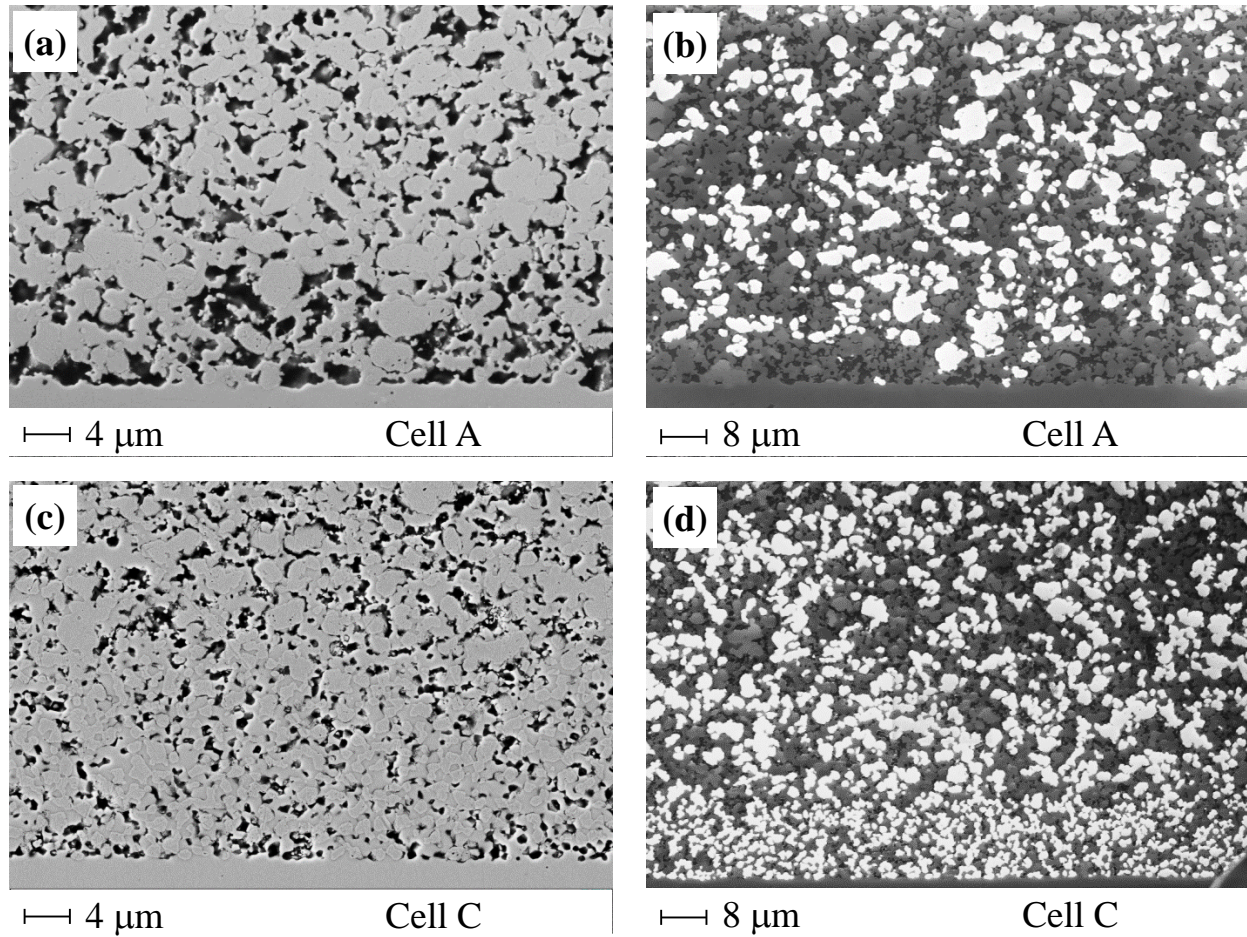


Figure 6: SEM images of the Ni/YSZ electrode-electrolyte interface for Cell A and Cell C after 1000 h and 2000 h of electrolysis test, respectively. SEM images b) and d) are low-voltage (0.9 kV) images detected using the in-lens detector [32].

3.4. Long-term test at increased current density: -1 A/cm^2 versus -1.25 A/cm^2 for identical cells

For test of Cell A, Cell B and Cell C the externally set galvanostatic electrolysis test conditions were identical while the fuel electrode microstructure was deliberately varying. Hereafter a galvanostatic electrolysis test was set-up, Cell D, using a sister-cell to Cell C. For this test, Cell D, the “externally” set test conditions were changed by increasing the current density to -1.25 A/cm^2 and increasing H_2O and H_2 flow to keep the same steam conversion as for previous tests. Figure 7 shows a comparison of the development of cell voltages, polarization resistances and ohmic resistances over time for the two identical cells, Cell C and Cell D. The discontinuity in cell voltage and polarization resistance for Cell D after approximately 120 h of testing is due to a minor adjustment of the $p(\text{H}_2\text{O})/p(\text{H}_2)$ ratio.

Figure 7 shows that the both the polarization resistance and ohmic resistance for Cell D does not resemble the trends over time that was observed for sister Cell C. The results from Cell D rather resembles the results obtained for Cell A and Cell B, which both had a coarser Ni-network compared to the microstructure of Cell C and Cell D.

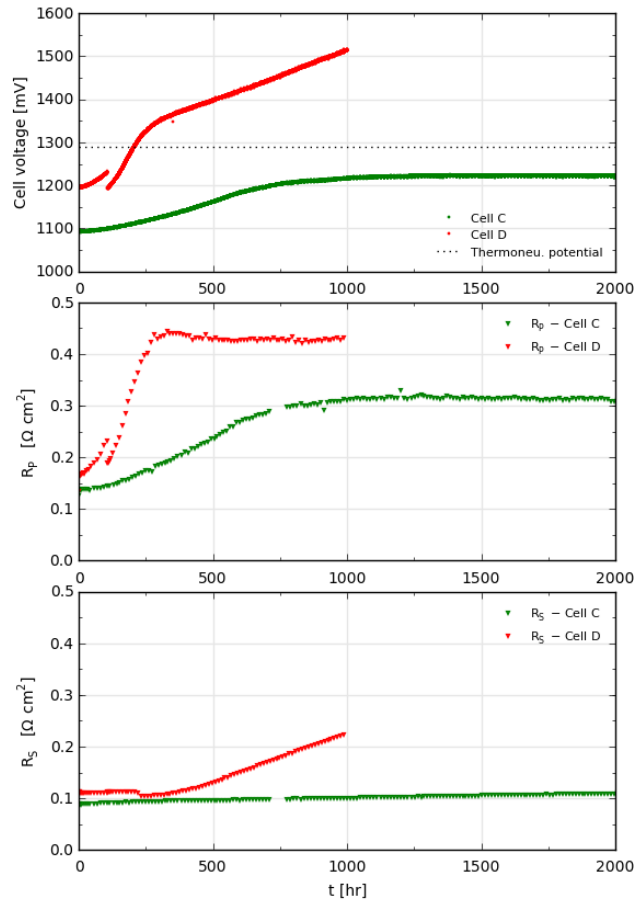


Figure 7: Comparison of cell voltage, R_p and R_s for galvanostatic long-term electrolysis testing of the two initially identical cells Cell C (-1 A/cm^2 for 2 kh) and Cell D (-1.25 A/cm^2 for 1 kh). Both tests were operated at $800 \text{ }^\circ\text{C}$, oxygen to the oxygen electrode, inlet $p(\text{H}_2\text{O})/p(\text{H}_2):90/10$ and 56 % steam conversion.

Figure 8 shows a comparison of IS recorded at start and after 1000 h of electrolysis testing for the two sister cells, Cell C and cell D. Not only does the polarization resistance attributed to electrochemical processes increase significantly more for Cell D than for Cell C, the Bode plot also reveals that the characteristic frequency for the largest polarization resistance contribution decreases down to a few hundred Hz for Cell D after 1000 h of testing at -1.25 A/cm^2 .

One-sided gas shifts (O_2/air for oxygen electrode and various $p(\text{H}_2\text{O})/p(\text{H}_2)$ on fuel electrode) and recording of IS was done before and after electrolysis testing. The analysis of differences in impedance spectra (ADIS [39]) showed that both the fuel and the oxygen electrode give rise to

impedance differences in the frequency range from 100-1000 Hz. Due to this frequency overlap of the impedance responses after long-term test for Cell D, a break-down of losses hardly provides fully trustworthy quantitative results for the individual electrode resistances.

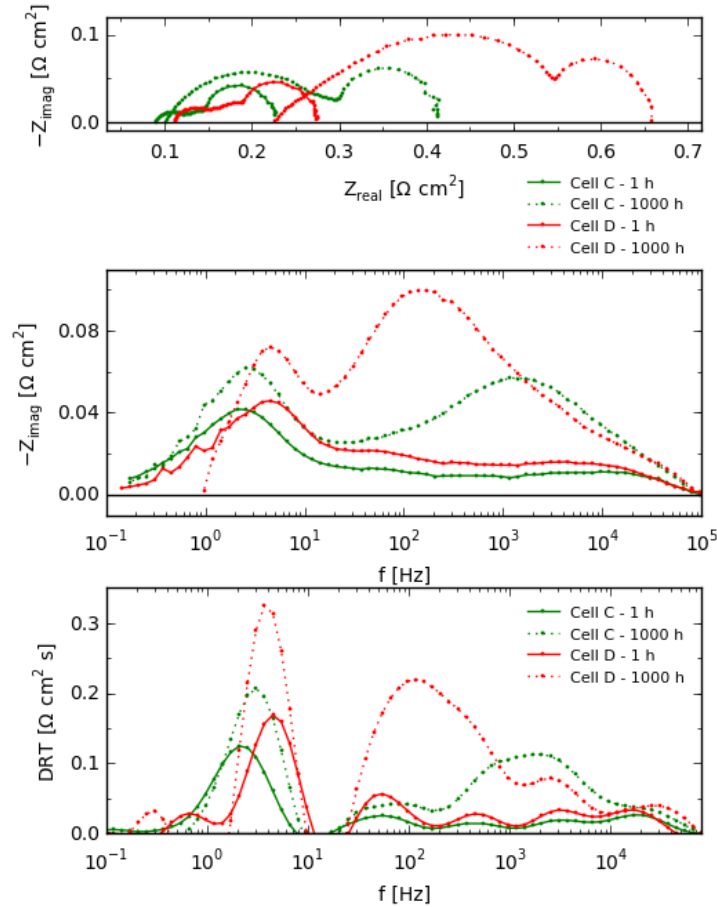


Figure 8: Nyquist (top), Bode (middle) and DRT plot (bottom) of IS recorded after 1 h and 1000 h for Cell C (-1 A/cm^2) and Cell D (-1.25 A/cm^2).

3.5. Microstructures of SOEC long-term tested at -1.25 A/cm^2

Figure 9 shows representative SEM images of Cell D after electrolysis test. Images in Figure 9a and Figure 9b are given at same magnifications as for the sister cell, Cell C (Figure 6c and Figure 6d). Figure 9a and Figure 9c can be compared with the images in Figure 1 for a “sister-cell” that was not long-term tested but simply reduced and used to investigate the initial microstructure (Cell C in Figure 1). From Figure 9a and Figure 9c it is evident that the Ni particles in the innermost $\sim 4 \mu\text{m}$ are not “locked” in the same way in the YSZ scaffold as it was initially (Figure 1), nor as it is in the outer part of the approximately $14 \mu\text{m}$ thick fuel electrode. In this inner-part of the fuel electrode of Cell D the Ni particles are detached from the YSZ scaffold; which is observed as dark

rims around the Ni particles (marked by red arrows in Figure 9d). Furthermore, breakage of Ni-Ni paths can also be observed in this inner-part of the fuel electrode (marked by blue squares in Figure 9c and Figure 9d). Comparing low-voltage in-lens images of Cell C (Figure 6d) and Cell D (Figure 9b) it is observed that there is a lack of Ni in percolating network in the “row” of Ni particles closest to the electrolyte for Cell D. However the total loss of Ni particles in general (not just the percolating of the Ni particles) for this inner part of the fuel electrode of Cell D seem less pronounced when compared to e.g. Cell A (Figure 6a) which had an increased number of larger pores most likely due to Ni migration. In this perspective, the microstructure of Cell D can be viewed as “pre-state” of the microstructural degradation observed for Cell A; as the Ni network in Cell D seem “loose” in the structure, but the Ni particles have not migrated to any larger extent.

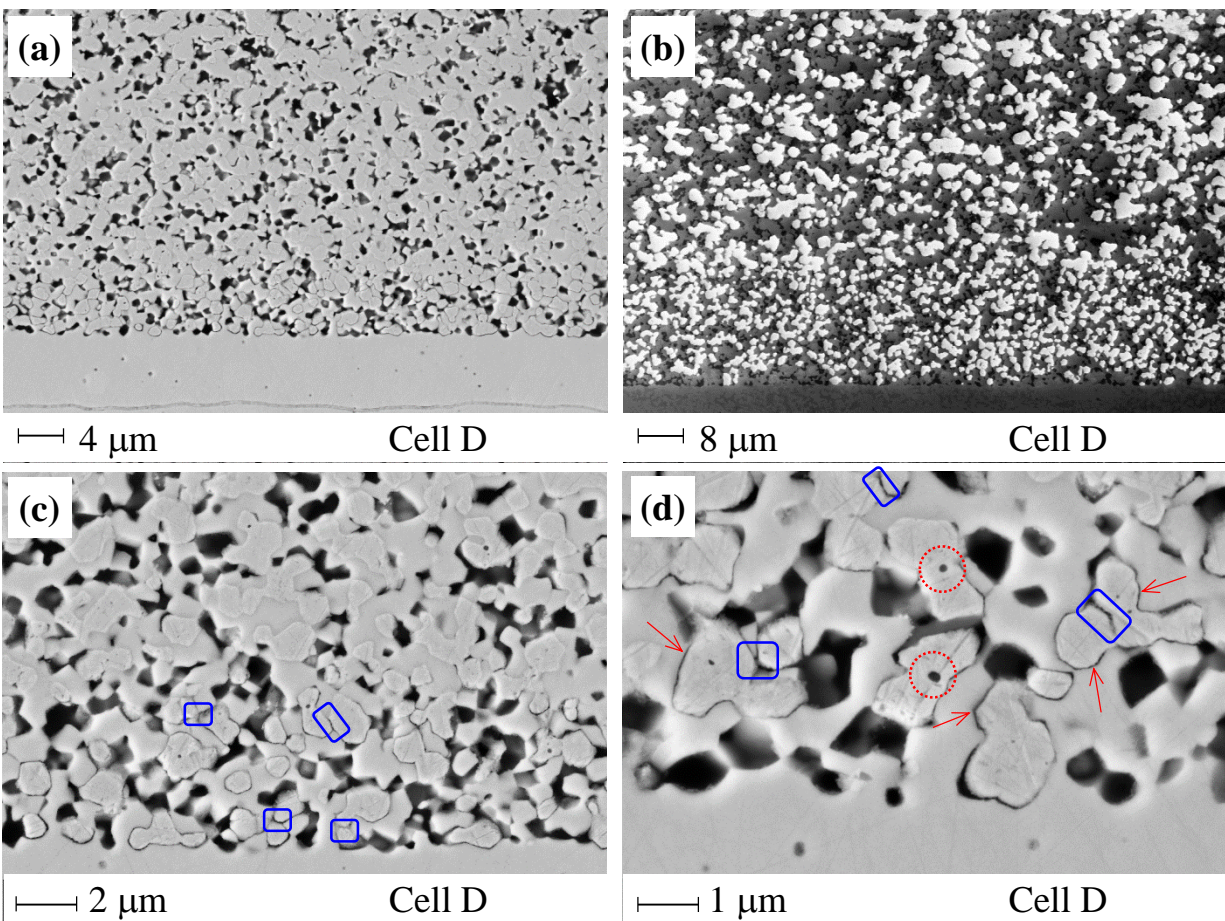


Figure 9: SEM images of the Ni/YSZ electrode-electrolyte interface for Cell D after 1000 h of electrolysis testing at -1.25 A/cm^2 . SEM images. Image b) is an in-lens low-voltage SEM image [32]. Blue squares in c) and d) highlight examples of lost Ni-Ni contact while red arrows highlights lost Ni-YSZ interface and red circles mark inclusions of silica-containing impurities in Ni [13,21].

4. Discussion

SOEC will typically be operated at rather high temperature (700-900 °C) and high partial pressure of steam (e.g. $p(\text{H}_2\text{O}) \sim 0.9 \text{ atm}$) at the fuel electrode inlet; conditions which will typically lead to mobility of Ni (e.g. via evaporation of $\text{Ni}(\text{OH})_x$ species [40]) and coarsening of Ni particles [41]. Nevertheless, the results presented in this work show that not only from an initial performance point of view (via increased TPB density) but also from a long-term stability point of view, it is advantageous to decrease the Ni particle size. Even though it seems counter intuitive, Cell C with the finest structured fuel electrode of the three investigated and long-term tested cells provide long-term stable operation at high current (-1 A/cm^2) and high inlet $p(\text{H}_2\text{O})$. Based on the IS during electrolysis testing and the microstructural changes upon long-term electrolysis testing we hypothesize that the following parameters play a key role in obtaining the optimal Ni/YSZ microstructure for Ni/YSZ based electrodes for steam electrolysis and for choice of operating conditions to avoid irreversible long-term degradation:

1. Decrease the particles size.
2. Ensure well-mixed and well-dispersed phases.
3. “Pack” the Ni/YSZ electrode as dense as the NiO allows, i.e. make the NiO-YSZ as close to 100 % density as possible.
4. Select test conditions based on electrode overpotential

Regarding point 1; the decreased particle size will lead to higher TPB density and thereby decreased overpotential for a given current density, which has shown to be an important parameter for long-term stability. Furthermore, matching the particle sizes of the different phases enables optimal mixing and dispersion of the three phases; Ni, YSZ and porosity.

Regarding point 2; for the electrode with well-dispersed phases, the YSZ skeleton can act as a hindrance for Ni migration/restrict Ni migration e.g. as confirmed via test with increased share of YSZ skeleton in the fuel electrode [37].

Regarding point 3; making the Ni/YSZ electrode as dense as the NiO reduction allows correspond to a theoretical pore fraction of 21.8 % for a Ni/YSZ electrode having a volume fraction of Ni/YSZ of 40/60 as applied in this work. This low porosity was obtained for Cell B, Cell C and Cell D reported here and no sign of gas diffusion problems were encountered at the chosen test conditions as the 300 μm thick support layer for all cells had a higher porosity. Previous 3D-reconstructions of similar Ni-stabilized zirconia electrodes have shown that electrodes having same phase fractions, similar PSDs and even comparable percolating TPB densities can have significantly different critical pathway radii for the Ni network, tortuosity for the percolating Ni path and significant differences in the number of percolating paths from the electrode/electrolyte interface to the outer circuit. These parameters were shown to affect the electrochemical performance significantly [22]. Based on those results and the observation of the microstructural changes in Cell D we therefore hypothesize that also the necking between Ni-Ni particles and the Ni-YSZ

interface area per electrode volume are important structural characteristics for the long-term stability of the Ni/YSZ electrode. These microstructural features can be optimized by “closest packing” of the Ni/YSZ structure. The loss of percolation in the Ni-network in the innermost part of the electrode in principle corresponds to increasing the thickness of the electrolyte layer; unfortunately with a very porous YSZ layer. This lead to the observed significant increase in the ohmic resistance for Cell A, Cell B and Cell D.

Cell A is not only more porous in the microstructure from a starting point compared to the other cells but also it is worth noticing that the electrode of Cell A is simply the same microstructure and chemical composition as the support layers for all cells. This means that the development of IS and microstructure for Cell A provides information about the expected degradation behavior for cells like Cell A and Cell D when tested long enough (few thousand hours more) that the break-up of the Ni-network and Ni migration has moved outwards to the border between the active fuel electrode and the support layer. In this perspective, results from Cell A shows that the support layer as expected can act as active fuel electrode but a degradation behavior similar to the one observed for the active fuel electrode of Cell B and Cell D is observed. In this context a supplementary test could be performed with a cell having a microstructure like Cell A but applying a Ni/8YSZ for the entire support layer. However, to process such cell, processing steps (among them sintering profile) need to be reconsidered.

Regarding point 4: the long-term electrolysis test results presented here point to the fact that the local overpotential (which is also the driving force for the local current density at TPB), rather than the externally set test conditions such as overall current density, that is a key parameter for the onset of the irreversible and almost linear long-term ohmic resistance caused degradation of the Ni/YSZ. For technological relevant full cells like the ones tested in this work, it is the overall fuel electrode overpotential during electrolysis testing that can be quantified via IS. The sum of R_{ion} and $R_{Ni/YSZ,TPB}$ provides an estimate of the overall electrochemical resistance for the active fuel electrode, from which the electrochemically related fuel electrode overpotential, $\eta_{Ni/YSZ}$, can be calculated and such parameter can be used to estimate the threshold for on-set of the irreversible and almost linear long-term degradation. For Cell A and Cell B the sum of R_{ion} and $R_{Ni/YSZ,TPB}$ is $\sim 0.10 \Omega\text{cm}^2$ ($\eta_{Ni/YSZ} \sim 100 \text{ mV}$) at start of electrolysis test and increases to slightly above $0.30 \Omega\text{cm}^2$ ($\eta_{Ni/YSZ} \sim 300 \text{ mV}$) within the first 500 h of testing. In contrast; Cell C starts out with a $R_{ion}+R_{Ni/YSZ,TPB}$ of $\sim 0.04 \Omega\text{cm}^2$ ($\eta_{Ni/YSZ} \sim 40 \text{ mV}$) and even after 2000 h of testing it has only reached $0.16 \Omega\text{cm}^2$ ($\eta_{Ni/YSZ} \sim 160 \text{ mV}$). An accurate breakdown of losses for the electrochemical processes' contribution to the polarization resistance during test for Cell D was not possible due to frequency overlapping contributions. However, a *rough* estimate for the fuel electrode overpotential can be found by considering the polarization resistance in the frequency range down to approximately 10 Hz and then subtract values for $R_{LSCC/CGO}$ and $R_{GasDiff}$ found for Cell C. This estimates fuel electrode overpotentials of $\eta_{Ni/YSZ} \sim 70 \text{ mV}$ at start of test of Cell D and $\eta_{Ni/YSZ} \sim 350$

mV already after 500 h of test. This illustrates that the three test (Cell A, Cell B and Cell D) even though having significantly different initial electrode microstructure, all have comparable fuel electrode overpotentials of 300-350 mV at which point the fuel electrode resistance stabilized. At this high electrode overpotential the irreversible and almost linear ohmic resistance increase becomes the dominating cause of cell degradation. These results suggest a fuel electrode overpotential “threshold” for breakage of the percolating Ni-network between 160 mV and 300 mV. Determining the critical fuel electrode overpotential for onset of this irreversible Ni/YSZ degradation can in turn be used to adjust to proper and “long-term-stability”-wise safe operating conditions; by tuning conditions such as temperature, gas composition, steam conversion and/or current density.

However; this overpotential threshold (which govern the local current density), for initiation of breakage of the Ni-network in the fuel electrode could vary e.g. with varying level of impurities, which will segregate to grain boundaries and interfaces [42–44] and possibly depend on microstructural parameters such as the ratio between particle sizes and critical pathway radius [37]. The results also highlights the importance of optimization of the microstructure for Ni/YSZ based fuel electrodes for SOEC, not only for initial performance but also for the long-term stability of the electrodes. Electrode microstructures can thereby be designed for more specific target operation of the SOEC. For example, electrodes designed to be stable at high current densities (fine particles sizes and dense structure) or produced cheaper by employing a more coarse structure will be acceptable for operating at lower current densities or higher temperatures.

The results presented here also emphasize the importance of long-term testing and illustrate how structural optimization of the well-known Ni/YSZ electrode can lead to technological relevant low long-term degradation rates. Figure 10 - inspired by Schefold and co-workes [38] - illustrates the importance in decreasing the long-term degradation rate from e.g. around 2 %/kh as reported by Schefold and co-workes [38] and Corre and Brisse [45] to the long-term degradation rate of 0.3-0.4 %/kh reported here for Cell C at similar test conditions.

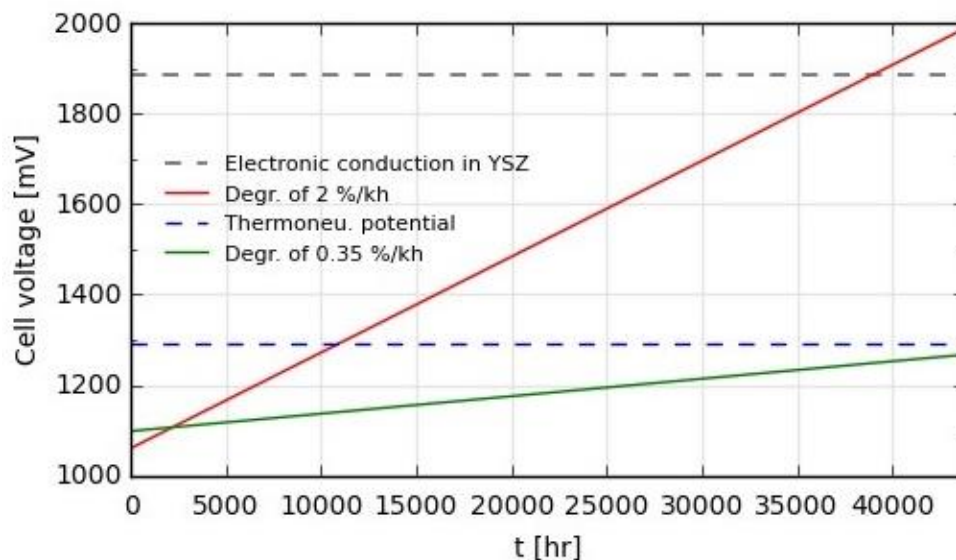


Figure 10: Sketch of cell voltage development during long-term degradation at 800 °C and -1 A/cm² for SOEC having degradation rates of 2 %/kh and 0.35 %/kh; inspired by degradation rates reported here for Cell C and previously reported by Schefold and co-workers [38].

5. Conclusion

From the results presented here, we conclude that:

- 1) A microstructure optimized Ni/YSZ SOEC electrode has been produced to reach a degradation rate for a full SOEC as low as 0.3-0.4 %/kh at 800 °C, -1 A/cm², p(H₂O)/p(H₂) ratio of 90/10 and steam conversion degree of 56 %. This long-term degradation rate predicts a life-time exceeding 5 years of operation below/around thermoneutral potential.
- 2) Though counter-intuitive, the optimal Ni/YSZ microstructure resulting in the most Ni-network robust Ni/YSZ electrode for electrolysis at high current and high p(H₂O) is an electrode which has the following properties: As dense as possible; as fine PSDs as possible; well dispersed and size matched PSDs for the different phases.
- 3) The electrode overpotential is the key parameter for the onset of the irreversible Ni-network-breakage-related degradation leading to significant ohmic resistance increase for the Ni/YSZ-electrode based SOEC.

6. Acknowledgement

The authors acknowledge colleagues at DTU Energy for technical assistance and fruitful discussions especially Mr H. Henriksen, Mrs M. Davodi, Mrs. P. H. Nielsen, Dr. P. S. Jørgensen and Dr. C. Graves. Furthermore, the authors would like to acknowledge the financial support from the projects “Solid Oxide Electrolysis for Grid Balancing” (Energinet.dk project no 2013-1-12013) and “Towards Solid Oxide Electrolysis Plants in 2020” (Energinet.dk project no. 2015-1-12276).

7. References

- [1] S.D. Ebbesen, S.H. Jensen, A. Hauch, M.B. Mogensen, *Chem. Rev.* 114 (2014) 10697–734.
- [2] S.H. Jensen, C. Graves, M. Mogensen, C. Wendel, R. Braun, G. Hughes, Z. Gao, S.A. Barnett, *Energy Environ. Sci.* 8 (2015) 2471–2479.
- [3] A. Hauch, S.H. Jensen, J.B. Bilde-Soerensen, M. Mogensen, *J. Electrochem. Soc.* 154 (2007) A619.
- [4] C. Graves, S.D. Ebbesen, S.H. Jensen, S.B. Simonsen, M.B. Mogensen, *Nat. Mater.* 14 (2015) 239–44.
- [5] A. Hauch, *Solid Oxide Electrolysis Cells – Performance and Durability*, PhD Thesis, Technical University of Denmark, 2007.
- [6] R. Knibbe, M.L. Traulsen, A. Hauch, S.D. Ebbesen, M. Mogensen, *J. Electrochem. Soc.* 157 (2010) B1209.
- [7] M. Chen, Y.-L. Liu, J.J. Bentzen, W. Zhang, X. Sun, A. Hauch, Y. Tao, J.R. Bowen, P.V. Hendriksen, *J. Electrochem. Soc.* 160 (2013) F883–F891.
- [8] F. Tietz, D. Sebold, A. Brisse, J. Schefold, *J. Power Sources* 223 (2013) 129–135.
- [9] G. Corre, A. Brisse, *ECS Trans.* 68 (2015) 3481–3490.
- [10] P. Hjalmarsson, X. Sun, Y.-L. Liu, M. Chen, *J. Power Sources* 262 (2014) 316–322.
- [11] X. Zhou, K. Sun, J. Gao, S. Le, N. Zhang, P. Wang, *J. Power Sources* 191 (2009) 528–533.
- [12] A. Hauch, F. Karas, K. Brodersen, M. Chen, in: *Proc. 11th Eur. SOFC SOE Forum*, 2014, p. 88.
- [13] C. Chatzichristodoulou, M. Chen, P.V. Hendriksen, T. Jacobsen, M.B. Mogensen, *Electrochim. Acta* 189 (2016) 265–282.
- [14] P.H. Larsen, K. Brodersen, *Reversible Solid Oxide Cell Producing Method Involves Sintering Multilayer Structure after Laminating Anode Support Layer on Top of Anode Layer*, US2008124602-A1; JP2008130568-A; EP1930974-A1; CN101242003-A; CA2611362-A1; KR2008047282-A; KR966845-B1, 2008.
- [15] J. Hjelm, M. Soegaard, R. Knibbe, A. Hagen, M. Mogensen, in: *ECS Trans.*, ECS, 2008, pp. 285–299.
- [16] M.J. Jørgensen, M. Mogensen, *J. Electrochem. Soc.* 148 (2001) A433–A442.
- [17] S. Ramousse, M. Menon, K. Brodersen, J. Knudsen, U. Rahbek, P.H. Larsen, *Ecs Trans.* 7 (2007) 317 – 327.
- [18] A. Hauch, C. Birkl, K. Brodersen, P.S. Jørgensen, *Proc. - 10th Eur. Solid Oxide Fuel Cell Forum Chapter 8* (2012) 62–71.
- [19] S.H. Jensen, A. Hauch, P. V Hendriksen, M. Mogensen, *J. Electrochem. Soc.* 156 (2009) B757.
- [20] S.D. Ebbesen, C. Graves, A. Hauch, S.H. Jensen, M. Mogensen, *J. Electrochem. Soc.* 157 (2010) B1419.
- [21] A. Hauch, S.D. Ebbesen, S.H. Jensen, M. Mogensen, *J. Electrochem. Soc.* 155 (2008) B1184.
- [22] P.S. Jørgensen, S.L. Ebbenhøj, A. Hauch, *J. Power Sources* 279 (2015) 686–693.
- [23] S.H. Jensen, *Solid Oxide Electrolyser Cell*, PhD Thesis, Technical University of Denmark, 2006.
- [24] C. Graves, *Ravdav* (2012) Data analysis software, Ver 0.97.
- [25] H. Schichlein, A.C. Muller, M. Voigts, A. Krugel, E. Ivers-Tiffée, *J. Appl. Electrochem.* 32 (2002) 875–882.

- [26] V. Sonn, A. Leonide, E. Ivers-Tiffée, *J. Electrochem. Soc.* 155 (2008) B675–B679.
- [27] A. Kromp, A. Leonide, A. Weber, E. Ivers-Tiffée, *J. Electrochem. Soc.* 158 (2011) B980–B986.
- [28] T. Ramos, J. Hjelm, M. Mogensen, *J. Electrochem. Soc.* 158 (2011) B814–B824.
- [29] J. Nielsen, J. Hjelm, *Electrochim. Acta* 115 (2014) 31–45.
- [30] S. Primdahl, M. Mogensen, *J. Electrochem. Soc.* 146 (1999) 2827–2833.
- [31] S. Primdahl, M. Mogensen, *J. Electrochem. Soc.* 145 (1998) 2431–2438.
- [32] K. Thydén, Y.-L. Liu, J.B. Bilde-Sørensen, *Solid State Ionics* 178 (2008) 1984–1989.
- [33] A. Hauch, P.S. Jørgensen, K. Brodersen, M. Mogensen, *J. Power Sources* 196 (2011) 8931–8941.
- [34] J.F.B. Rasmussen, A. Hagen, *J. Power Sources* 191 (2009) 534–541.
- [35] A. Hauch, A. Hagen, J. Hjelm, T. Ramos, *J. Electrochem. Soc.* 161 (2014) F734–F743.
- [36] E.E. Underwood, *Am. Soc. Test. Mater.* 504 (1972) 3–38.
- [37] K. Brodersen, A. Hauch, M. Chen, J. Hjelm, *Durable Fuel Electrode*, Patent application no Ep15181381.3, 2015.
- [38] J. Schefold, A. Brisse, F. Tietz, *J. Electrochem. Soc.* 159 (2012) A137.
- [39] S.H. Jensen, J. Hjelm, A. Hagen, M. Mogensen, in: W. Vielstich, H. Yokokawa, H.A. Gasteiger (Eds.), *Handb. Fuel Cells - Fundam. Technol. Appl. Vol. 6*, John Wiley & Sons, Ltd, 2009, pp. 1090–1102.
- [40] R. Knibbe, A. Hauch, J. Hjelm, S.D. Ebbesen, M. Mogensen, *Green* 1 (2011) 141–169.
- [41] J. Sehested, J.A.P. Gelten, S. Helveg, *Appl. Catal. A-General* 309 (2006) 237–246.
- [42] M.S. Schmidt, K. V Hansen, K. Norrman, M. Mogensen, *Solid State Ionics* 179 (2008) 1436–1441.
- [43] K. Vels Jensen, S. Primdahl, I. Chorkendorff, M. Mogensen, *Solid State Ionics* 144 (2001) 197–209.
- [44] D. Wiedenmann, A. Hauch, B. Grobéty, M. Mogensen, U.F. Vogt, *Int. J. Hydrogen Energy* 35 (2010) 5053–5060.
- [45] G. Corre, A. Brisse, *ECS Trans.* 68 (2015) 3481–3490.